Progress In Electromagnetics Research, Vol. 115, 259–287, 2011

CHARACTERISTIC BASIS FUNCTIONS OF THE ENERGY RADIATION PATTERN OF A SPARSE TRUE TIME DELAY ARRAY

A. Shlivinski

Department of Electrical and Computer Engineering
Ben-Gurion University of the Negev, Beer-Sheva 84105, Israel

Abstract—A set of characteristic basis functions of the energy radiation pattern for a true-time-delay array of equi-spaced elements radiating a pulsed/transient wave-field was derived. This set is determined by the array layout and by the set of excitation waveforms that can be used to expand the actual excitation pulse. It is established that the characteristic basis function set spans the mapping of the square amplitudes of the discrete Fourier transform of the excitation coefficients to the energy radiation pattern. This mapping is further used to analyze array performance and re-examine the term array sparsity. Additional use of this set can be found in synthesizing an array radiation pattern to meet prescribed requirements.

1. INTRODUCTION

The far-field time-dependent radiation pattern of a true time delay (TTD) array antenna (or antennas for non-sinusoidal excitation signals, see, e.g., [1]) depends on a set of two coordinates: angular ($\hat{\boldsymbol{r}}$ – 2D vector in an angular domain) and temporal (t). In applications concerning the net energy radiated by the array, one is interested in the energy radiation pattern (ERP) of the array rather than the time-dependent pattern. As such, the ERP provides a simpler representation by only one coordinate, i.e., the angular, of the radiation pattern. Nevertheless, in terms of the observability of certain kinematic characteristics of the TD array, it was already shown, see, e.g., [2, 3] that they also have an impact on the ERP. Therefore, the ERP is a valid tool for TTD array kinematic analysis.

Received 15 February 2011, Accepted 30 March 2011, Scheduled 1 April 2011
Corresponding author: Amir Shlivinski (amirshli@ee.bgu.ac.il).

In a previous publication [2, 3] a kinematic analysis of the TTD array was performed with the radiated field (in the time domain) and via its ERP. This analysis yielded a representation of the radiation pattern by the array's set of radiated beams that are structured on an angular predetermined lattice. Once the TTD array parameters are given, this beam lattice and the corresponding beams can be easily determined. The direct dependence of the set of radiated beams on both the layout (geometry) of the array and on the actual element's excitation pulse somewhat limits its use in (*i*) analysis of general ERP characteristics and (*ii*) synthesis of the ERP. To this end, an alternative approach to the representation of the ERP is taken in the present manuscript that entails the decomposition of the ERP into a weighted summation of characteristic basis functions (CBF). These CBFs describe the transformation (mapping) between the set of array exciting sources and the corresponding far-field ERP. This transform, in turn, gives rise to a general set of functions that can be used to analyze/synthesize and optimize the array's ERP properties. For an equi-spaced linear array, the decomposition of the ERP into its corresponding CBFs is carried out using an eigen-decomposition of Toelplitz and circulant matrixes [4–6]. The resulting set of CBFs encapsulates the possible kinematic characteristics of the array and therefore is complementary to [2, 3]. In particular it provides a new, and refined, point of view on the TTD array's *sparsity* and gives additional analysis tools for obtaining some bounds and characteristics of the array's performance upon synthesizing a TTD array. Furthermore, the CBF formulation is uniformly applicable for signals ranging from that of a short-pulsed type to that of a time harmonic (TH) type.

The manuscript is organized as follows. Problem formulation in a step–by–step manner is treated in Section 2 where the array's layout and excitation parameters, in addition to its observable parameters that are further used to construct the CBFs, are reviewed. The CBF set for the general case is derived and analyzed in Section 3 followed by an example for the basic single pulsed waveform radiation case in Section 4. Section 4 provides also a discussion on the properties of ERP expansion by the CBF set, their bounds and on different conditions of array sparsity. Additionally, Section 4 provides an example of several array realizations, their corresponding CBF sets and ERPs in order to clarify the discussion and show the applicability in antenna theory analysis/design. Section 5 comprises a summary and concluding remarks.

2. PROBLEM FORMULATION AND PRELIMINARIES

In the following section, problem formulation is put forward by considering the radiating array layout, the array's elements model, and the observation setup.

2.1. Layout

2.1.1. Physical Layout

Let us consider a one-dimensional (1D) linear array of N radiating elements aligned along the z-axis with inter-element spacing d. Without loss of generality, all array elements have the same source to far-field transfer function (termed effective height) $h^t(\hat{\boldsymbol{r}}, t) = H(\hat{\boldsymbol{r}})D(t)$ in transmission, where t is a temporal coordinate, $\hat{\boldsymbol{r}} = (v\hat{\boldsymbol{\rho}}, u)$ with $\hat{\boldsymbol{\rho}} = \hat{\boldsymbol{x}}\cos\phi + \hat{\boldsymbol{y}}\sin\phi$, $u = \cos\theta$, and $v = \sin\theta$, $0 \le \theta \le \pi$, $0 \le \phi \le 2\pi$. Here, $H(\hat{\boldsymbol{r}})$ is an angular radiation pattern in the $\hat{\boldsymbol{r}}$ direction and $D(t)$ is a time dependent operator [†]. Such decomposition of h^t is useful in treating many types of small radiating elements (transducers) that have a multipolar type of radiation pattern with $D(t)$ as a differential operator (see, e.g., in antenna theory [7–10]. For the extended type of transducer, $h^t(\hat{\boldsymbol{r}}, t)$ can be decomposed to a summation of products of the angular and temporal functions (see, e.g., the discussion in[10]). Additionally, without loss of generality the array's main radiation beam is set here in the x direction.

2.1.2. Excitation Signal Set

The incident excitation signal at the terminal of the nth radiating element, $n = 0, 1, \ldots, N-1$ is given by:

$$s_n(t) = \sum_{p=0}^{P} \left[s_{np}^{(r)} \varphi(t - t_p) - s_{np}^{(i)} \check{\varphi}(t - t_p) \right], \qquad t_p = p\bar{t} \tag{1}$$

where $s_{np}^{(r)}, s_{np}^{(i)} \in \mathbb{R}$, $n = 0, 1, \ldots, N-1$ and $p = 0, 1, \ldots, P$, are two sequences of excitation coefficients. The window $\varphi(t)$ is an essentially time-limited and frequency-band-limited real pulse-shaped waveform with a prescribed central frequency (see the discussion below). The window $\check{\varphi}(t) = \mathrm{P.V.}\frac{1}{\pi t} \circledast \varphi(t)$ is the Hilbert transform of $\check{\varphi}(t)$, where $\circledast$ represents the convolution integral

[†] The derivation, here, is performed within scalar antenna theory, i.e., for acoustical sources or transducers radiating in a 2 dimensional space (x, z) or as projection of an electromagnetic field on the corresponding aperture E-plane or H-plane. An extension to the full vectorial case can easily be carried out following similar lines of derivation.

$\left([a(\cdot) \circledast b(\cdot)]\,(t) = \int dt' a(t') b(t-t')\right)$, and P.V. is the principal value of the integration. The delay term $\bar{t}$ is the temporal duration between successive contributions.

The excitation signal given in Eq. (1) can be used to (i) represent a sequence of distinct pulses (*pulse-train*) of the form $s_{np}^{(r)}\varphi(t) - s_{np}^{(i)}\check{\varphi}(t)$, whenever $\bar{t}$ is greater than the single pulse duration (pulsed-width), see, e.g., [3]. In such a case $\bar{t}$ is the pulse repetition duration (with PRF $= \bar{t}^{-1}$). Moreover, the signal representation in (1) corresponds, then, to a broad class of the *quadrature modulated* type of signal. (ii) Alternatively, by maintaining a proper balance between the excitation coefficients $s_{np}^{(r)}$ and $s_{np}^{(i)}$, Eq. (1) can generally be used to represent a signal-waveform by its temporal samples, in which case $\varphi(t)$ is an interpolation window and $\bar{t}$ is the sampling interval that satisfies the Nyquist sampling criterion.

One should note that a compact representation of the signal in the brackets in Eq. (1) could be obtained by resorting to the analytic signals notation $\overset{+}{s}_n(t)$, where

$$\begin{aligned} \overset{+}{s}_n(t) &= \sum_{p=0}^{P} s_{np}\overset{+}{\varphi}(t-t_p), \\ s_{np} &= s_{np}^{(r)} + i s_{np}^{(i)}, \qquad \overset{+}{\varphi}(t) = \varphi(t) + i\check{\varphi}(t), \end{aligned} \tag{2}$$

$i = \sqrt{-1}$ and $s_n(t) = \mathrm{Re}\{\overset{+}{s}_n(t)\}$.

2.2. Radiated Field

Combining the excitation model in (1) with the radiating elements model $h^t(\hat{\boldsymbol{r}}, t)$, the nth element analytic transient radiation field is given by $e_n(\hat{\boldsymbol{r}}, t) = \mathrm{Re}\{\overset{+}{e}_n(\hat{\boldsymbol{r}}, t)\}$, with:

$$\overset{+}{e}_n(\hat{\boldsymbol{r}}, t) = \frac{1}{4\pi r} H(\hat{\boldsymbol{r}})\overset{+}{f}_n(\hat{\boldsymbol{r}}, \tau), \qquad \overset{+}{f}_n(\hat{\boldsymbol{r}}, \tau) = \sum_{p=0}^{P} s_{np}\overset{+}{\psi}(\tau - t_p), \tag{3}$$

the radiated pulse analytic waveform is given by $\overset{+}{\psi}(\tau) = \left[D(\cdot) \circledast \overset{+}{\varphi}(\cdot)\right](\tau)$, $\boldsymbol{r} = (x, y, z)$, with $r = |\boldsymbol{r}|$, and the retarded time $\tau = t - r/c$, with c as the wave propagation speed.

Similar to (3), the array's time dependent far-field is given by $\overset{+}{E}(\boldsymbol{r}, t) = \frac{1}{4\pi r}\overset{+}{F}(\hat{\boldsymbol{r}}, \tau)$, where $\overset{+}{F}(\hat{\boldsymbol{r}}, \tau)$ is the corresponding analytic counterpart of the transient radiation pattern that is obtained by

an aggregation the properly delayed far-fields of the individual array elements to give

$$\overset{+}{F}(\hat{\boldsymbol{r}},\tau)=H(\hat{\boldsymbol{r}})\overset{+}{F}_a(\hat{\boldsymbol{r}},\tau),\ \overset{+}{F}_a(\hat{\boldsymbol{r}},\tau)=\overset{+}{F}_a(u,\tau)=\sum_{n=0}^{N-1}\overset{+}{f}_n(\tau+ndc^{-1}u). \quad (4)$$

In Eq. (4), $\overset{+}{F}_a(u,\tau)$ denotes the analytic counterpart of the radiation pattern of the array itself without the angular "filtering" effect of the elements' angular pattern. Since the discussion focuses mainly on the analysis of the array's kinematic properties, inter-element coupling (the interaction between the array elements) is therefore neglected (for details regarding the effect of coupling in TD arrays see [9]).

2.2.1. Signal Characteristics and Bandwidth Regimes

In view of (3), the element's far-field $\overset{+}{e}_n(\tau)$ is also a pulsed-waveform, however, due to the $D(t)$ operator, some of its characteristics may differ from those of its source $\overset{+}{s}_n(t)$. Since $D(t)$ may contain derivations and $\overset{+}{\varphi}(t)$ has a pulsed shape, it follows that $\overset{+}{\psi}(t)$ (and $\psi(t)=\mathrm{Re}\{\overset{+}{\psi}(t)\}$) in (3) can be modeled as a modulated pulsed-waveform $\psi(t)\approx r_0(t)\cos(\omega_0 t+\phi)$, where $r_0(t)$ is a base-band pulsed shaped window with an effective pulse-width (say T), $\omega_0=2\pi/T_0$, and ϕ is a delay phase. The choice of $r_0(t)$, ω_0, and ϕ depends on the temporal characteristics of $\psi(t)$. This modeling of $\psi(t)$ does not limit the discussion to a certain type of pulsed excitations, as will be shown below; rather, it allows some of the unique properties attributed to NB, QM and UWB/SP excitation regimes to be quantified (for additional discussion, see, [3]).

Next, it should be noted that based on the ratio T/T_0, "pulsed excitation" can be classified as one of three types (see, e.g., [2, 3]) (*i*) *NB* for $T/T_0\gtrsim\mathcal{O}(1)$, where the signal's characterization is dominated by the carrier frequency (thus, TH considerations may be used, with the periodicity T_0 identified as a carrier frequency); (*ii*) *UWB/SP* for $T/T_0\lesssim 0.2$, where the signal is dominated by the short pulsed envelope $r_0(t)$; or (*iii*) the intermediate range of $0.2\lesssim T/T_0\lesssim 1$, termed the *quasi-monochromatic (QM)* regime, where the signal's attributes are characterized by an interplay between the NB (carrier) and the UWB/SP (modulation) properties, see the discussion below.

2.3. Energy Radiation Pattern

Following the introduction of the array's far-field in Eq. (4), the ERP is presented as the primary observable used to derive the CBF set. To

this end, let an energy radiation pattern be defined as the $\mathcal{L}_2$ norm of the far-field, on an *infinite temporal observation window* , via:

$$\mathcal{E}(\hat{\boldsymbol{r}}) = (4\pi r)^2 \left\| E(\boldsymbol{r},t) \right\|_2^2 = \int_\infty d\tau \left| F(\hat{\boldsymbol{r}},\tau) \right|^2 = \frac{1}{2} \overset{+}{\mathcal{R}}_{F}(\tau;\hat{\boldsymbol{r}})\big|_{\tau=0}. \quad (5a)$$

where $\overset{+}{\mathcal{R}}_{F}(\tau;\hat{\boldsymbol{r}})$ is the autocorrelation function of $\overset{+}{F}(\hat{\boldsymbol{r}},\tau)$ and is given by

$$\begin{aligned} \overset{+}{\mathcal{R}}_{F}(\tau;\hat{\boldsymbol{r}}) &= \left[\overset{+}{F}(\hat{\boldsymbol{r}},-\tau) \right]^* \circledast \overset{+}{F}(\hat{\boldsymbol{r}},\tau) \\ &= \int_\infty dt \, \left[\overset{+}{F}(\hat{\boldsymbol{r}},t-\tau/2) \right]^* \overset{+}{F}(\hat{\boldsymbol{r}},t+\tau/2) \end{aligned} \quad (5b)$$

with the asterisk denoting complex conjugation.

Inserting Eq. (3) with (4) into Eq. (5) yields the expression for the energy radiation pattern in terms of the distinct elements contribution [3]:

$$\begin{aligned} \mathcal{E}(\hat{\boldsymbol{r}}) &= |H(\hat{\boldsymbol{r}})|^2 \mathcal{E}_a(\hat{\boldsymbol{r}}), \\ \mathcal{E}_a(\hat{\boldsymbol{r}}) &= \mathcal{E}_a(u) = \frac{1}{2} \sum_{n=0}^{N-1} \sum_{m=0}^{N-1} \overset{+}{\mathcal{R}}_{nm} \left((n-m) c^{-1} du \right), \end{aligned} \quad (6a)$$

where $\overset{+}{\mathcal{R}}_{nm}[\tau] = [\overset{+}{f}_n(\hat{\boldsymbol{r}},-\tau)]^* \circledast \overset{+}{f}_m(\hat{\boldsymbol{r}},\tau)$ is the temporal cross correlation between $\overset{+}{e}_n$ and $\overset{+}{e}_m$, given explicitly by the double summation

$$\begin{aligned} \overset{+}{\mathcal{R}}_{nm}(\tau) &= \sum_{p=0}^{P} \sum_{q=0}^{P} s_{np}^* s_{mq} \overset{+}{\mathcal{R}}_{\psi} \left(\tau + (p-q)\bar{t} \right), \\ \overset{+}{\mathcal{R}}_{\psi}(\tau) &= \left[\overset{+}{\psi}(\tau) \right]^* \circledast \overset{+}{\psi}(-\tau). \end{aligned} \quad (6b)$$

Noting that due to rotational symmetry around the array ($\hat{\boldsymbol{z}}$ axis, in ϕ), $\mathcal{E}_a(\hat{\boldsymbol{r}})$ is effectively a parameter of, only, $u = \cos\theta$ therefore $\mathcal{E}_a(\hat{\boldsymbol{r}}) = \mathcal{E}_a(u)$ in Eq. (6a).

The decomposition of $\mathcal{E}(\hat{\boldsymbol{r}})$ in Eq. (6a) by using $\mathcal{E}_a(\hat{\boldsymbol{r}})$ which is a function of the array's physical layout, the excitation pulses ($s_n(t)$), and the elements' temporal transfer function $D(t)$ implies that $\mathcal{E}_a(\hat{\boldsymbol{r}})$ preserves the core characteristics of the array and as such can be identified as an energy *array factor*. Thus, continued use of $\mathcal{E}_a(\hat{\boldsymbol{r}})$ instead of $\mathcal{E}(\hat{\boldsymbol{r}})$ also preserves the array's kinematic characteristics (see Figs. 3, 5 and 7 below for some typical examples and in [3]). To this end, Eqs. (6a) and (6b) can be rearranged in a matrix format

as $\mathcal{E}_a(u) = \frac{1}{2}\mathbb{1}_N^T \mathbf{R}\, \mathbb{1}_N$, where $\mathbf{R}$ is an $N \times N$ matrix whose nmth element is given by $[\mathbf{R}]_{nm} = \overset{+}{\mathcal{R}}_{nm}[(n-m)\mu]$, $\mu = dc^{-1}u$, and $\mathbb{1}_N$ is an N dimensional column vector whose elements equal 1. Similarly, $\overset{+}{\mathcal{R}}_{nm}(\tau) = \boldsymbol{s}_n^\dagger \mathbf{R}_\psi(\tau)\boldsymbol{s}_m$, where $\mathbf{R}_\psi(\tau)$ is a $(P+1)\times(P+1)$ matrix whose pqth element is $[\mathbf{R}_\psi]_{pq}(\tau) = \overset{+}{\mathcal{R}}_\psi[\tau + (p-q)\bar{t}]$, $\mathbf{s}_{n,m}$, are two $(P+1)$ dimensional column vectors with $[\mathbf{s}_n]_p = s_{np}$ and $[\mathbf{s}_m]_q = s_{mp}$, respectively, and $\dagger$ denotes the Hermitian transpose. Noting that the matrix $\mathbf{R}_\psi$ is a Toeplitz matrix will play a key role in the derivation of the CBF set below. Concatenating $\mathbf{s}_n$, $n = 0, \ldots, N-1$, into an $N(P+1)$ column vector $\mathbf{s} = \left[\mathbf{s}_0^\dagger\ \mathbf{s}_1^\dagger \ldots \mathbf{s}_{N-1}^\dagger\right]^\dagger$ shows that Eq. (6a) can, conveniently, be given by,

$$\mathcal{E}_a(u) = \frac{1}{2}\mathbf{s}^\dagger\, \mathbf{R}_\mathcal{E}(u)\, \mathbf{s}, \tag{7a}$$

where $\mathbf{R}_\mathcal{E}$ is a block Toeplitz matrix with $N \times N$ blocks each of size $(P+1)\times(P+1)$. Therefore,

$$\mathbf{R}_\mathcal{E}(u) = \begin{bmatrix} \mathbf{R}_\psi(0) & \mathbf{R}_\psi(-\mu) & \ldots & \mathbf{R}_\psi(-(N-1)\mu) \\ \mathbf{R}_\psi(\mu) & \mathbf{R}_\psi(0) & \ldots & \vdots \\ \vdots & \vdots & \ddots & \vdots \\ \mathbf{R}_\psi((N-1)\mu) & \mathbf{R}_\psi((N-2)\mu) & \ldots & \mathbf{R}_\psi(0) \end{bmatrix}. \tag{7b}$$

Regarding Eq. (5b) it should be noted that the properties of the autocorrelation function of analytic signals implies that $\left[\overset{+}{\mathcal{R}}_F(-\tau;\hat{\boldsymbol{r}})\right]^* = \overset{+}{\mathcal{R}}_F(\tau;\hat{\boldsymbol{r}})$. Therefore, it renders the matrixes $\mathbf{R}_\psi$ and, consequently, block-matrix $\mathbf{R}_\mathcal{E}$, Hermitian matrixes. Furthermore, a key property of the ERP is its positiveness, i.e., both $\mathcal{E}(u)$ and $\mathcal{E}_a(u) \geq 0$ for all $\hat{\boldsymbol{r}}$ (synonymously u), which further implies, via Eq. (7), that the matrix $\mathbf{R}_\mathcal{E}(u)$ is also a positive defined matrix.

2.4. Problem Statement

The derivation in Section 2.3 giving Eq. (7a) concludes the problem setup by formulating a convenient mathematical representation for the ERP. Furthermore, it demonstrates that all ERP characteristics are governed by a concise set of attributes of $\mathbf{R}_\mathcal{E}(u)$. Therefore, to characterize the array performance by, for example a CBF set, the characteristic functions of the matrix $\mathbf{R}_\mathcal{E}(u)$ should be further analyzed.

3. EIGEN DECOMPOSITION AND CBF DERIVATION

Following the problem statement in Section 2.4 and in view of Eq. (7a), array performance can be investigated by analyzing the matrix $\mathbf{R}_{\mathcal{E}}(u)$ characteristics to obtain the CBF set. A convenient set of u-dependent (or $\hat{\boldsymbol{r}}$-dependent) characteristics of $\mathbf{R}_{\mathcal{E}}$ is obtained by applying its eigen-decomposition. Recalling that $\mathbf{R}_{\mathcal{E}}$ has a canonical structure of a block Toeplitz matrix with Toeplitz blocks, obtaining an explicit expression of its u-dependent eigen-decomposition is impractical. However, embedding the $\mathbf{R}_{\mathcal{E}}$ blocks into a larger circulant matrix[‡] with circulant blocks yields closed form expressions [up to a discrete Fourier transform, (DFT), operation] to the associated eigen-system (vectors and values) [4–6]. This course of action will be pursued next with demonstrations in Section 4.

3.1. Embedding $\mathbf{R}_{\mathcal{E}}$ into a Circulant Matrix

To derive an eigen-decomposition of $\mathbf{R}_{\mathcal{E}}$, $\mathcal{E}_a$ in Eq. (7) is reformulated as a vector-matrix-vector product with a circulant matrix with circulant blocks. This reformulation involves the embedding of the Toeplitz blocks $\mathbf{R}_{\psi}(\tau)$ of $\mathbf{R}_{\mathcal{E}}$ into a larger circulant matrix $\mathbf{C}_{\psi}(\tau)$. To this end, let $\mathbf{C}_{\psi}(\tau)$ and $\widetilde{\boldsymbol{s}}_n$ comprise a $(2P+1)\times(2P+1)$ circulant matrix and a $2P+1$ zero-padded vector, respectively, that are defined by

$$\mathbf{C}_{\psi}(\tau)=\operatorname{circ}\left\{\mathbf{v}(\tau)\right\},\qquad \widetilde{\boldsymbol{s}}_n=\left[\boldsymbol{s}_n^{\dagger}\;\;\mathbb{0}_P^{\dagger}\right]^{\dagger}, \tag{8a}$$

where circ is a shorthand notation for circulant matrix, whose first row is the vector,

$$\begin{aligned}\mathbf{v}(\tau)=\Big[&\overset{+}{\mathcal{R}}_{\psi}(\tau),\overset{+}{\mathcal{R}}_{\psi}(\tau-\bar{t}),\ldots,\overset{+}{\mathcal{R}}_{\psi}(\tau-\bar{t}P),\\ &\overset{+}{\mathcal{R}}_{\psi}(\tau+\bar{t}P),\overset{+}{\mathcal{R}}_{\psi}(\tau+\bar{t}(P-1))\ldots\overset{+}{\mathcal{R}}_{\psi}(\tau+\bar{t})\Big]\end{aligned} \tag{8b}$$

and $\mathbb{0}_P$ is a zero column vector of dimension P, giving

$$\mathbf{C}_{\psi}(\tau)=\begin{bmatrix}\mathbf{R}_{\psi}(\tau) & \mathbf{C}_{\psi}^{(12)}(\tau)\\ \mathbf{C}_{\psi}^{(21)}(\tau) & \mathbf{C}_{\psi}^{(22)}(\tau)\end{bmatrix}, \tag{8c}$$

where $\mathbf{C}_{\psi}^{(12)}$ and $\mathbf{C}_{\psi}^{(21)}$ are two rectangular Toeplitz matrixes of size $(P+1)\times P$ and $P\times(P+1)$, respectively, and $\mathbf{C}_{\psi}^{(22)}$ is a Toeplitz matrix of dimension $P\times P$. Note that this embedding suggests that $\overset{+}{\mathcal{R}}_{nm}(\tau)=\widetilde{\boldsymbol{s}}_n^{\dagger}\mathbf{C}_{\psi}(\tau)\widetilde{\boldsymbol{s}}_m$ [see Eq. (6b)].

[‡] For the definition of a circulant matrix see [4].

To achieve similar embedding for the block Toeplitz matrix in Eq. (7b), let $\widetilde{\mathbf{s}}$ be a zero padded vector of dimension $(2N-1)(2P+1)$ defined by

$$\widetilde{\mathbf{s}} = \left[\widetilde{\boldsymbol{s}}_0^{\dagger}\ \widetilde{\boldsymbol{s}}_1^{\dagger} \ldots \widetilde{\boldsymbol{s}}_{N-1}^{\dagger}\ \mathbb{0}^{\dagger}\right]^{\dagger}, \tag{9a}$$

where $\mathbb{0}$ is a column vector of zeroes of dimension $(N-1)(2P+1)$ and $\mathbf{C}_{\mathcal{E}}$ be the $(2N-1)(2P+1) \times (2N-1)(2P+1)$ block circulant matrix with circulant blocks that is defined as

$$\begin{aligned}\mathbf{C}_{\mathcal{E}} = \text{bcirc}\,\{&\mathbf{C}_{\psi}(0), \mathbf{C}_{\psi}(-\mu), \ldots, \mathbf{C}_{\psi}(-(N-1)\mu),\\ &\mathbf{C}_{\psi}((N-1)\mu), \mathbf{C}_{\psi}((N-2)\mu) \ldots \mathbf{C}_{\psi}(\mu)\}\,,\end{aligned} \tag{9b}$$

where bicirc is a shorthand notation for a block circulant matrix formed by the circular shifts of the blocks within the curly brackets in Eq. (9b) [4, 6]. Using the newly derived $\widetilde{\mathbf{s}}$ and $\mathbf{C}_{\mathcal{E}}$, the ERP of Eq. (7a) is reformulated as

$$\mathcal{E}_a(u) = \frac{1}{2}\widetilde{\mathbf{s}}^{\dagger}\,\mathbf{C}_{\mathcal{E}}(u)\,\widetilde{\mathbf{s}}. \tag{9c}$$

It should be noted that the Hermitian property of $\mathbf{R}_{\mathcal{E}}$ is inherited by $\mathbf{C}_{\mathcal{E}}$.

Although the reformulation of $\mathcal{E}_a$ in Eq. (7a) into a large system to give Eq. (9c) seems to complicate the discussion. However, since $\mathbf{C}_{\mathcal{E}}(u)$ is a block circulant with circulant blocks matrix its eigen-decomposition is readily available in closed form for any u [4–6], as will be discussed next.

3.2. Eigen-decomposition of $\mathbf{C}_{\mathcal{E}}(u)$

A favorable property of the eigen-decomposition of a circulant and block circulant with circulant block matrixes is their analytic simplicity [4–6]. Moreover, the eigenvectors of these circulant matrixes depend exclusively on the circular structure of the matrix and not on the matrix entries. Consequently, all circulant/block-circulant with circulant block matrixes of the same structure (i.e., block size and number of blocks) have the *same eigenvectors*, which are known analytically, while the values of the matrixes' entries determine the associated eigenvalues. This property of the eigenvectors is a key point in the present CBF derivation, because as the parameter u changes, it sets different entries for the matrix $\mathbf{C}_{\mathcal{E}}(u)$. Since $\mathbf{C}_{\mathcal{E}}(u)$ maintains it structure (block size and number of blocks) independent of u, it has *u-independent eigenvectors* while the functional dependence on the spectral (angular) parameter u is shifted into the eigenvalues. Recall that given a matrix and its eigenvectors, the corresponding eigenvalues are obtained by matrix-vector multiplications. Hence, the

u dependence of $\mathcal{E}_a$ is governed by the set of u-dependent eigenvalues of $\mathbf{C}_\varepsilon(u)$, which are further identified as the CBF's of the array (as will be discussed below).

To formulate the above discussion, let an eigen-decomposition of $\mathbf{C}_\varepsilon(u)$ be given by a summation of products of rank-1 matrixes, which may concisely be written as,

$$\mathbf{C}_\varepsilon(u) = \sum_{j\in\mathcal{J}}\sum_{n\in\mathcal{N}} \lambda_{n,j}(u)\mathbf{c}_{n,j}\mathbf{c}_{n,j}^\dagger, \tag{10a}$$

where $\mathcal{N} = 0,1,\ldots,2N-2$, $\mathcal{J} = 0,1,\ldots,2P$, $\{\mathbf{c}_{n,j}\}$ is the set of eigenvectors, and $\{\lambda_{n,j}(u)\}$ is the corresponding set of eigenvalues. Due to the block-circulant with circulant blocks structure of $\mathbf{C}_\varepsilon(u)$, the set of eigenvectors $\{\mathbf{c}_{n,j}\}$ is determined as follows [4, 6]: let

$$\rho_j = \exp\left(i\frac{2\pi}{2P+1}j\right), \qquad r_n = \exp\left(i\frac{2\pi}{2N-1}n\right), \tag{10b}$$

be two sets of $2P+1$ and $2N-1$ roots of 1 (uniformly distributed on the unit circle in the complex plain) and define the sets of two column vectors with unit euclidian norm:

$$\boldsymbol{\rho}_j = \frac{1}{\sqrt{2P+1}}\begin{bmatrix} 1 \\ \rho_j \\ \rho_j^2 \\ \vdots \\ \rho^{2P} \end{bmatrix}, \qquad \boldsymbol{r}_n = \frac{1}{\sqrt{2N-1}}\begin{bmatrix} 1 \\ r_n \\ r_n^2 \\ \vdots \\ r^{2N-2} \end{bmatrix}. \tag{10c}$$

For a given index $\{n,j\}$, an eigenvector $\mathbf{c}_{n,j}$ is obtained by the Kronecker product [§]

$$\mathbf{c}_{n,j} = \boldsymbol{r}_n \otimes \boldsymbol{\rho}_j. \tag{10d}$$

Once the eigenvectors have been acquired, given a spectral parameter u, the corresponding eigenvalues $\{\lambda_{n,j}(u)\}$ can be obtained as follows. Since $\mathbf{C}_\varepsilon(u)$ is Hermitian, its eigenvectors are orthogonal, which further yield, following Eq. (10a), the u-dependent eigenvalue:

$$\lambda_{n,j}(u) = \mathbf{c}_{n,j}^\dagger \mathbf{C}_\varepsilon(u)\mathbf{c}_{n,j}, \qquad n\in\mathcal{N}, \quad j\in\mathcal{J}. \tag{11}$$

Next, inserting the eigen-decomposition of $\mathbf{C}_\varepsilon(u)$ given in Eq. (10a) into the array's ERP of Eq. (9c) yields the expression for the energy radiation pattern decomposition in terms of the weighted summation of the elements of an *eigen*-set of spectral (angular) characteristic functions $\lambda_{n,j}(u)$:

$$\mathcal{E}_a(u) = \frac{1}{2}\sum_{j\in\mathcal{J}}\sum_{n\in\mathcal{N}} \lambda_{n,j}(u)\left|\hat{\widetilde{\mathbf{s}}}_{n,j}\right|^2, \qquad \hat{\widetilde{\mathbf{s}}}_{n,j} = \mathbf{c}_{n,j}^\dagger \widetilde{\mathbf{s}}. \tag{12}$$

[§] For the definition of the Kronecker product, see [11].

where $|\widehat{\widetilde{\mathbf{s}}}_{n,j}|^2$ are the summation weights. Examples of the use of Eq. (12) are given in Section 4.

3.2.1. DFT Formulation

Noting that the two sets of vectors $\boldsymbol{\rho}_j$ and $\boldsymbol{r}_n$, $\{(n,j)|n \in \mathcal{N}, j \in \mathcal{J}\}$, are basis elements for the 1D DFT of a sequences of lengths $2P+1$ and $2N-1$, respectively, a concise generalization of Eq. (11) and of the summation weights in Eq. (12) for all $\{(n,j)$ pairs can be obtained in terms of a two-dimensional (2D) DFT. To that end, let the eigenvalues be arranged in a matrix $[\mathbf{\Lambda}(u)]_{n,j} = \lambda_{n,j}(u)$, and define the matrix

$$\mathbf{V}(u) = [\,\mathbf{v}^{\dagger}(0)\ \mathbf{v}^{\dagger}(-\mu)\ldots \\ \mathbf{v}^{\dagger}(-(N-1)\mu)\ \mathbf{v}^{\dagger}(N-1)\mu)\ \mathbf{v}^{\dagger}((N-2)\mu)\ldots\mathbf{v}^{\dagger}(\mu)\,]^{\dagger},$$

for which $\mathbf{v}(\tau)$ was set in Eq. (8b). Note that both $\mathbf{\Lambda}$ and $\mathbf{V}$ matrixes are of dimension $(2N-1)\times(2P+1)$. The eigenvalues matrix $\mathbf{\Lambda}(u)$ is obtained as a normalized 2D DFT of $\mathbf{V}$, of lengths $2P+1$ along the rows and $2N-1$ along the columns, such that $\lambda_{n,j} = \boldsymbol{r}_n^T \mathbf{V} \boldsymbol{\rho}_j$, where the superscript ^{T} denotes matrix transpose. Similarly, the set of coefficient $\widehat{\widetilde{\mathbf{s}}}_{n,j}$ is obtained up to a redundant phase by a normalized two-dimensional DFT of the matrix $\mathbf{S} = [\mathbf{s}_0\,\mathbf{s}_1\,\ldots\,\mathbf{s}_{N-1}]$ of size $(P+1)\times N$ by embedding it as an upper-left block into a larger $(2P+1)\times(2N-1)$ matrix $\widetilde{\mathbf{S}}$ whose other elements are zero. Note that this embedding is the equivalent of zero padding for achieving an increased resolution in DFT (see, e.g., [12]).

3.3. The Eigenvalues Set and the CBFs

Following the discussion in the previous sections, *given* (i) a physical array layout and (ii) a set of possible excitation waveforms. The set of u dependent eigenvalues $\{\lambda_{n,j}(u)\}$, $\{(n,j)|n \in \mathcal{N}, j \in \mathcal{J}\}$, of $\mathbf{C}_{\mathcal{E}}(u)$ is obtained by a 2D DFT (Section 3.2.1), such that $\mathcal{E}_a(u) \in \text{span}\{\lambda_{n,j}(u)\}$, Eq. (12).

An interpretation of the role of the set of $\{\lambda_{n,j}(u)\}$ is obtained by viewing Eq. (12) as a mapping operation between a set of positive excitation coefficients $|\widehat{\widetilde{\mathbf{s}}}_{n,j}|^2$ and the radiation pattern $\mathcal{E}_a$. As such, the elements of $\{\lambda_{n,j}(u)\}$, $\{(n,j) \mid n \in \mathcal{N}, j \in \mathcal{J}\}$ spectrally map ("distribute") the energy in the excitation into the far-field. Due to their role as building blocks of the ERP, the elements of the eigenvalues set $\{\lambda_{n,j}(u)\}$ are identified as the *set of CBFs with respect to the spectral (angular) parameter.*

3.3.1. The CBF Set and the Attainable ERPs

Once the CBF set has been defined, the resulting properties of the spectral (angular) domain spanned by the CBF set $\{\lambda_{n,j}(u)\}$ and its relation to the set of all attainable, physically valid, radiation patterns $\mathcal{E}_a(u)$ is discussed next:

(i) A key point is whether a single element of the CBF set, say $\lambda_{n',j'}(u)$ with $\{(n',j') \mid n' \in \mathcal{N}, j' \in \mathcal{J}\}$, is a valid and realizable ERP?
In general, the elements of the set $\{\lambda_{n,j}(u)\}$, $\{(n,j) \mid n \in \mathcal{N}, j \in \mathcal{J}\}$ *do not satisfy any orthogonality with respect to* u as part of their reconstruction. Therefore, one possibility of realizing a single CBF ERP realization, $\mathcal{E}_a(u) = \lambda_{n',j'}(u)$, is for the set of expansion coefficients in Eq. (12) to satisfy $\hat{\widetilde{\mathbf{s}}}_{n,j} = \sigma_{n',j'}\delta_{(n',j')(n,j)}$ where $\sigma_{n',j'}$ is an amplitude and $\delta_{(n',j')(n,j)}$ is the Kronecker delta. Because the spectral coefficients $\hat{\widetilde{\mathbf{s}}}_{n,j}$ and spatial coefficients (i.e., the elements of $\widetilde{\mathbf{S}}$) are related via a 2D DFT, satisfying $\hat{\widetilde{\mathbf{s}}}_{n,j} = \sigma_{n',j'}\delta_{(n',j')(n,j)}$, therefore, requires that the elements of $\widetilde{\mathbf{S}}$ have the same absolute magnitude (different than zero) with some progressive phase, which defy the construction of $\widetilde{\mathbf{S}}$ by "zero padding" $\mathbf{S}$. Consequently, a single CBF ($\lambda_{n',j'}(u)$) by itself is *not a realizable ERP*.
Furthermore, generally, the CBF elements $\lambda_{n,j}(u)$ are *not non-negative* in the observation range $|u| < 1$ [see, e.g., the example in Eq. (13)]. Since $\mathcal{E}_a(u)$ is an energy radiation pattern, it is defined as being *non-negative*, and therefore, a single CBF-ERP realization is unattainable.

(ii) Attaining a non-negative u-dependent function that belongs to the span of the CBF set is not sufficient by itself to suggests that it can be a valid radiation pattern. This argument follows from Eq. (12) which requires that, in addition, the expansion coefficients $\left|\hat{\widetilde{\mathbf{s}}}_{n,j}\right|^2$ will be nonnegative (since they are the square of the absolute value of a generally complex coefficient).

(iii) Let $\mathcal{L}$ be the space spanned by the CBF set. An element $\ell(u) \in \mathcal{L}$ is generally given by $\ell(u) = \frac{1}{2}\sum_{j\in\mathcal{J}}\sum_{n\in\mathcal{N}} l_{n,j}\lambda_{n,j}(u)$ where $l_{n,j} \in \mathbb{C}$ [see Eq. (12)]. Let $\mathcal{P}$ be the set of all u-dependent non-negative functions, $\ell_{n,j}(u) > 0$. Additionally, let $\mathcal{P}^+$ be the set of all $\ell_{n,j}(u) \subset \mathcal{P}$ with $l_{n,j} \geq 0$. Finally, let $\mathcal{P}_\mathcal{E}$ be the set for which $l_{n,j} = \left|\hat{\widetilde{\mathbf{s}}}_{n,j}\right|^2$ [compare to Eq. (12)] where $\hat{\widetilde{\mathbf{s}}}_{n,j}$ are DFT coefficients of

some zero-padded excitation sequence. Following the construction of $\mathcal{L}$ and the cascading sets $\mathcal{P}$, $\mathcal{P}^+$ and $\mathcal{P}_\varepsilon$, a physically realizable radiation pattern satisfies $\mathcal{E}_a(u) \in \mathcal{P}_\varepsilon \subset \mathcal{P}^+ \subset \mathcal{P} \subset \mathcal{L}$. Therefore, the set of attainable ERPs is only a partition of the possible span of the CBF set. In an analysis problem where the set of excitations, $\{s_{np}\}$ in Eq. (1), is known, it always $\mathcal{E}_a(u) \in \mathcal{P}_\varepsilon \subset \mathcal{P}^+ \subset \mathcal{P} \subset \mathcal{L}$. However, in a synthesis problem of the radiation pattern to meet some prescribed characteristics or in an inverse source problem, it is important to address this cascading sets. These issues will be explored further elsewhere.

A demonstration of the CBF set for the simplest case of $P = 0$ follows.

4. DETAILED DEMONSTRATION: THE $P = 0$ CASE

The presentation in the previous sections is applicable to a general N-elements array and an excitation waveform that comprise a set of $P + 1$ basis waveforms. In this section, on the other hand, a detailed demonstration and discussion of the simple, basic, case of an N-elements array with a single waveform type of excitation ($P = 0$) is performed. This case is explored in order to gain some insight on the physical as well as the mathematical properties of the CBFs in connection to known transient antenna characteristics. The discussion is followed by demonstrations of some array realizations.

Given an N-elements array with an inter-element spacing d, let the eventual element's radiated waveform (see in Section 2.2) be $\psi(t) = r_0(t)\cos(\omega_0 t)$, where $\omega_0 = 2\pi/T_0$, $r_0(t)$ is a real valued base-band pulsed-shaped window of an effective width T and $\omega_0 T > 1$ (QM and NB regimes, see, e.g., [3]). Let the given range of parameters be set such that the associated analytic radiated waveform can be well approximated by $\overset{+}{\psi}(t) \simeq r_0(t)\exp(-i\omega_0 t)$.

Following the discussion in Section 2.3, the autocorrelation $\overset{+}{\mathcal{R}}_\psi(\tau) = [\overset{+}{\psi}(-\tau)]^* \circledast \overset{+}{\psi}(\tau) = \mathcal{R}_{r_0}(\tau)\exp(-i\omega_0\tau)$, where $\mathcal{R}_{r_0}(\tau) = r_0(-\tau) \circledast r_0(\tau)$, is the autocorrelation function of $r_0(t)$. Correspondingly, in view of Eqs. (6)-(8), $\mathbf{R}_\psi(\tau) = \mathbf{C}_\psi(\tau) = \mathbf{v}(\tau) = \overset{+}{\mathcal{R}}_\psi(\tau)$. Using $\mathbf{v}(\tau)$ to calculate the CBF set as is suggested in Section 3.2.1, it follows that $\mathbf{V} = \left[\overset{+}{\mathcal{R}}_\psi(0)\ \overset{+}{\mathcal{R}}_\psi(-\mu)\ \ldots\ \overset{+}{\mathcal{R}}_\psi(-(N-1)\mu)\ \overset{+}{\mathcal{R}}_\psi((N-1)\mu)\right.$ $\left.\overset{+}{\mathcal{R}}_\psi((N-2)\mu)\ \ldots \overset{+}{\mathcal{R}}_\psi(\mu)\right]$, and consequently, the set of CBFs is given by a 1D DFT vector $\mathbf{\Lambda}(u) = \mathcal{DFT}_{1\mathrm{D}}\{\mathbf{V}(u)\}$, giving $[\mathbf{\Lambda}(u)]_n = \lambda_n(u)$,

where:

$$\lambda_n(u) = \frac{1}{\sqrt{2N-1}} \sum_{k=1-N}^{N-1} \overset{+}{\mathcal{R}}_{\psi}(-k\mu) \exp\left(i\frac{2\pi k}{2N-1}n\right) \tag{13a}$$

$$= \frac{1}{\sqrt{2N-1}} \sum_{k=1-N}^{N-1} \mathcal{R}_{r_0}(k\mu) \exp\left(i\xi_n k\right), \tag{13b}$$

with $\mu = dc^{-1}u$, $\xi_n = \omega_0\mu + \frac{2\pi n}{2N-1}$ and $n \in \mathcal{N}$. Equation (13) gives the formal expression for the individual CBFs to be used to construct the ERP, which following Eq. (12) is given by $\mathcal{E}_a(u) = \frac{1}{2}\sum_{n=0}^{2N-2} \lambda_n(u) \left|\hat{\tilde{\mathbf{s}}}_n\right|^2$. Examples of the use of Eq. (13) for different array realizations is given in Figs. 1, 2, 4 and 6.

Since the excitation conditions range from the QM regime to the NB regime (and possibly to the extreme NB, i.e., TH), the CBFs of Eq. (13) and the array performance (ERP) can be discussed in view of two characteristics: (*i*) Kinematic (in Section 4.1), which is governed by physical parameterization (layout) and the signal carrier; (*ii*) Waveform-dynamic (in Section 4.2),which is governed by the pulsed characteristics (pulse waveform and duration). It should be emphasized that the resulting *kinematic characteristics* of the CBFs are *insensitive* to the change in the pulse-shaped window and therefore, are the same for the QM, NB, and TH regimes. The combined view of these two issues provides a general characteristic of the TTD array (and of the CBFs) in a complementary and somewhat generic manner than that in [2, 3] (see, e.g., the discussion on sparsity in Section 4.2.1).

4.1. Kinematic Considerations

Recalling that $r_0(t)$ is a real base-band pulse (bell) shaped window, it follows that $\mathcal{R}_{r_0}(\tau)$ is also a real bell shape function that is monotonically decaying for $\tau > 0$. It therefore follows via Eq. (13) that since $\mathcal{R}_{r_0}(\tau)$ is real, in general, $\lambda_n(u)$ peaks positively whenever the $2N-1$ contributions are phase-matched. This phase matching occurs for $\xi_n = 2\ell\pi$, with $\ell \in \mathbb{Z}$, thus giving a set of local peaks for the nth CBF at the spectral parameter:

$$u_{n,\ell} = \frac{cT_0}{d}\left(\ell - \frac{n}{2N-1}\right), \qquad n \in \mathcal{N}, \quad \ell \in \mathbb{Z}. \tag{14}$$

The set $\{u_{n,\ell} | \, n \in \mathcal{N}, \ell \in \mathbb{Z}\}$ defines the nodes of a lattice of spectral (angular) directions, denoted as the *CBF-lattice*, where the CBFs

obtain their peak (of a "main-lobe" type), which is independent of the actual pulsed waveform $r_0(t)$.

Once the CBF-lattice has been defined, the array's kinematic properties can be discussed based on the set of the nodes analyzed. Let $\mathcal{L}_n \subset \mathbb{Z}$, $n \in \mathcal{N}$ denote a partition of all the integers such that for a given CBF index n, $\ell \in \mathcal{L}_n$ if $|u_{n,\ell}| \leq 1$. Next define $\#_n$ as the support (number of elements) of $\mathcal{L}_n$. It follows that the inter element spacing (d) and carrier frequency ($\omega_0 = 2\pi/T_0$) determine the set of partitions $\mathcal{L}_n$, where three cases can be discussed and demonstrate for their effect on the kinematic properties of the ERP:

- **Empty partition ($\#_\mathbf{n} = \mathbf{0}$):** For an inter-element spacing d/cT_0 that is small enough it is possible to obtain an empty partition $\mathcal{L}_n = \emptyset$ ($\#_n = 0$) which implies that the peak of the "main (dominant) lobe" of the nth CBF resides outside the observation domain with $|u_{n,l}| > 1$. Alternatively, within the observation domain, the nth CBF makes a degenerate (small or negligible) contribution. This case suggests that due to an apparent spatial oversampling of the aperture, the effective number of degrees of freedom needed for the representation of the ERP is less than $2N-1$. Nevertheless, truncation of the weighted CBF summation in Eq. (12) to account for non-degenerate CBFs, introduces some error into the observation domain due to the "long tail" of the degenerate CBFs.

  For a demonstration of the CBF set for the "empty partition" case, let assume an array composed of 41 omni-directional radiating elements with $d/cT_0 = 0.25$, giving an array of size $D = 10cT_0$. Recall that cT_0 is the wavelength at the carrier frequency [3]. Additionally, the radiated signal by each of the elements, $\psi(t)$, is taken as a type of modulated Lorenzian pulse of duration T (i.e., $r_0(t) \sim (t^2 + (T/2)^2)^{-1}$), however other pulsed waveforms can also be used with minor changes in the results. Fig. 1 depicts a gray-scaled color-map layout of the CBF set, as calculated via Eq. (13a), as a function of u within the observation domain $|u| \leq 1$ for two excitation regimes: $T/T_0 \gg 1$ (NB excitation regime) in Fig. 1(a), and $T/T_0 = 0.75$ (QM excitation regime) in Fig. 1(b). The color scaling in the figures is linear with an amplitude normalization with respect to $\lambda_0(0)$. Note that the dark diagonal lines corresponds to the "main lobe" of the CBFs which for the $T/T_0 \gg 1$ (Fig. 1(a)) corresponds to the CBF set as expressed in Eq. (18) below. It is readily observed that CBFs with index between 20 and 60 have no "main lobe" within the observation domain which implies that these CBFs constitute an empty partition. This comes due to the dense packing of

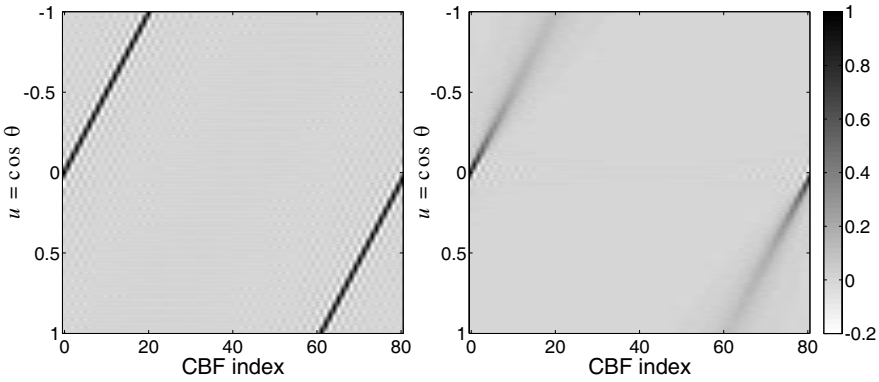

(a) $\frac{T}{T_0} >> 1$ (b) $\frac{T}{T_0} = 0.75$

Figure 1. A layout of the CBF set as a function of u for the "empty partition case" for a 41 elements array with $d/cT_0 = 0.25$ that is excited with a modulated Lorenzian pulsed waveform and for two cases: (a) $T/T_0 \gg 1$, i.e., NB excitation regime; (b) $T/T_0 = 0.75$, i.e., QM excitation regime.

the array $d/cT_0 < 0.5$ (see the discussion in Section 4.1.1). Comparing Figs. 1(a) and 1(b) demonstrates that the property of "empty partition" is invariant with the excitation regime while the magnitude and angular spreading of the CBFs depend on the excitation regime (see the additional discussion in Section 4.2).

- **More than one element partition ($\#_{\mathbf{n}} > 1$):** For an inter-element spacing d/cT_0 that is large enough, it is possible to obtain a CBF with more than one "dominant lobe" within the observation domain ($\#_n > 1$). In view of Eq. (12), the corresponding CBF contributes dominantly in more than one direction, thereby introducing ambiguity (on the main radiation direction, this ambiguity is somewhat resolved by using the waveform dynamic considerations of Section 4.2). This phenomenon is unwelcome, since it can lead to ERP with some grating-lobes (GL), see in Fig. 3 and [2, 3, 13].
  A demonstration of the "more than one element partition" case is given in Fig. 2 which depicts a color-map layout of the CBF set as calculated via Eq. (13a), as a function of u for a 6 elements array, array size $D = 10cT_0$ as in the previous case (but, here, $d/cT_0 = 2 > 1$) and the same excitation signal and scaling as in Fig. 1. The appearance of more than one "dominant lobe" (dark diagonal lines) within for $|u| \leq 1$ implies that this is indeed

the case for "more than one element partition". A comparison between the two excitation regimes (Fig. 2(a) for the NB regime and Fig. 2(b) for the QM regime) demonstrates, again, that the property of "more than one element partition" is invariant to the excitation regime while the magnitude and angular spreading of the CBFs strongly depends on the excitation regime (see the additional discussion in Section 4.2).

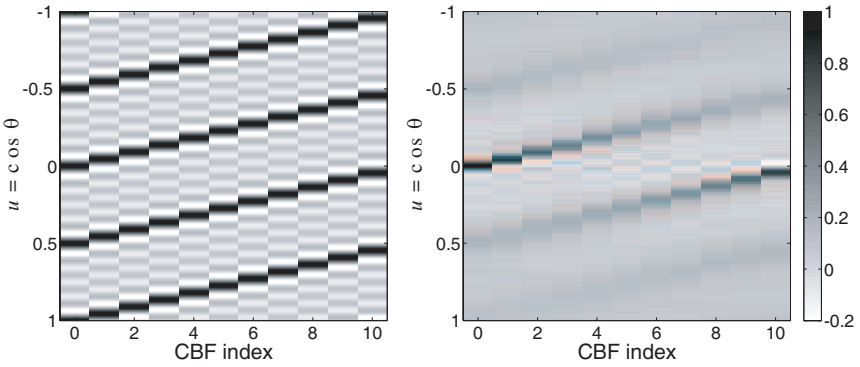

(a) $\frac{T}{T_0} >> 1$ (b) $\frac{T}{T_0} = 0.75$

Figure 2. As in Fig. 1 but for the "more than one element partition" case for a 6 elements array with $d/cT_0 = 2$, the total length of the array is $10cT_0$ (as used in Fig. 1).

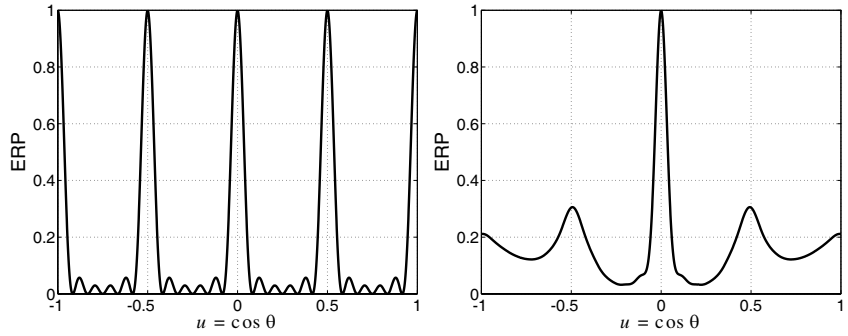

(a) $\frac{T}{T_0} >> 1$ (b) $\frac{T}{T_0} = 0.75$

Figure 3. The ERP for a uniformly excited array (equal s_{np} for all elements, see in (2)) with the same physical and waveform parameters that were used for the CBF layout in Fig. 2 for two cases: (a) $T/T_0 \gg 1$, i.e., NB excitation regime; (b) $T/T_0 = 0.75$, i.e., QM excitation regime.

Additionally, Fig. 3 depicts the ERP for a uniformly excited array (equal s_{np}, $p = 0$, with the same pulsed waveforms for all elements, see in (2)) and for the same physical and waveform parameters used for the calculation of the CBF layout in Fig. 2. The ERP was calculated by Eq. (12) for the two cases discussed in Fig. 2, i.e., NB excitation in Fig. 3(a) and the QM excitation in Fig. 3(b). One can clearly observe the appearance of GLs within the observation domain (more than one dominant lobe), as expected, since the inter-element spacing is grater than one wavelength at the carrier frequency ($d/cT_0 = 2$) and as a consequence of the identification of the CBFs in Fig. 2 as having "more than one element partition". The difference in the GLs' magnitude between the two cases depicted in Figs. 3(a) and 3(b) follows from the different excitation bandwidth (see the additional discussion in Section 4.2 and the detailed analysis in [3]).

- **One element partition ($\#_{\mathbf{n}} = \mathbf{1}$):** For the nth CBF that constitutes a partition $\mathcal{L}_n$ with support $\#_n = 1$ and one index term $l \in \mathbb{Z}$, the range of the inter-element spacing should be in the intersection of the following system of inequalities [that are derived from Eq. (14)]:

$$|u_{n_m,l}| \leq 1, \qquad |u_{n_m,l\pm1}| > 1, \tag{15}$$

where $n_m = 0, 1, \ldots, N-1$ is the "warped" index defined by

$$n_m = \begin{cases} n, & n = 0, 1, \ldots, N-1; \\ 2N-1-n, & n = N, N+1, \ldots 2N-2\ . \end{cases} \tag{16}$$

The first inequality in Eq. (15) rule out the non-degeneracy case while the second prohibits the ambiguity case of the n_mth CBF. Note that the warped index $n_m(n)$ accounts for the symmetry with respect to the index n of the CBFs. The solution of these inequalities yields a segment $D_{n_m} \in \mathbb{R}$ corresponding to the range of values for which the inter-element spacings of the nth CBF (denoted by $d/cT_0|_{n_m}$) form a partition with $\#_n = 1$:

$$\begin{aligned} &\left.\frac{d}{cT_0}\right|_{n_m} \in D_{n_m} = (D^l_{n_m}, D^h_{n_m}), \\ &D^l_{n_m} = \frac{n_m}{2N-1}, \quad D^h_{n_m} = 1 - \frac{n_m}{2N-1} \end{aligned} \tag{17}$$

where the lower bound $D^l_{n_m}$ comes from the non-degenerate condition and the upper bound $D^h_{n_m}$ comes from the unambiguity condition.

Following Eq. (17), the set of segments D_{n_m} satisfies the nesting condition $D_{n_m} \subset D_{n_m-1}$. This nesting condition suggests that if

$d/cT_0 \in D_m$ but $d/cT_0 \notin D_{m+1}$, then the partitions $\mathcal{L}_{n_m}$ for the $n_m \leq m$ CBFs will constitute $\#_{n_m} = 1$ while those for $n_m > m$ can either constitute $\# = 0$ if $d/cT_0 \in (0, D^l_{m+1})$ or $\# > 1$ if $d/cT_0 \in (D^h_{m+1}, \infty)$.

A demonstration of the "one element partition" is shown in Fig. 4 which depicts the CBF layout (as in Figs. 1 and 2) for an array with 21 elements, array of size $D = 10cT_0$, as in the previous two cases (but $d/cT_0 = 0.5$) with the same excitation and scaling as in Fig. 1. The appearance of only one "dominant lobe" for $|u| \leq 1$ implies that the case of "one element partition" was achieved for *all CBFs*. A comparison between the two excitation regimes (Fig. 4(a) for the NB regime and Fig. 4(b) for the QM regime), again, demonstrates that the partitioning property is invariant to the excitation regime while the magnitude and angular spreading of the CBFs strongly depends on the excitation regime (see the additional discussion in Section 4.2). Note, also, that the array physical and excitation parameters that were used in Fig. 1, above, renders the CBFs of index less than 20 and greater than 60 to belong to the "one element partition" (while the other CBFs belong to the "empty partition" as was discussed above).

Finally, Fig. 5 depicts the ERP for the uniformly excited array and for the same physical and waveform parameters that are used for the two CBF layouts in Fig. 4. It is noted that since the inter-element spacing is $d/cT_0 = 0.5$ (i.e., exactly half

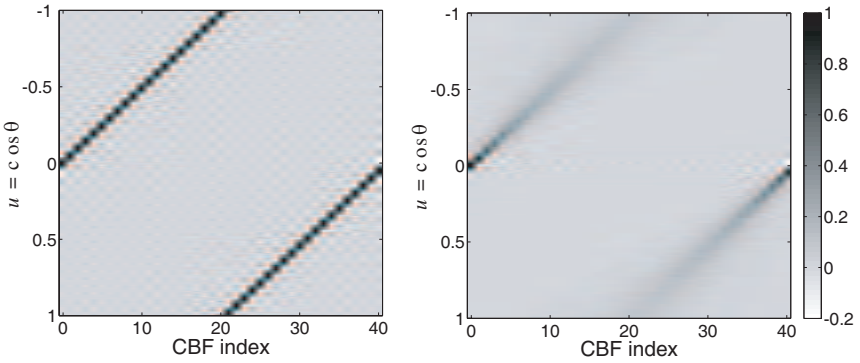

(a) $\frac{T}{T_0} \gg 1$ (b) $\frac{T}{T_0} = 0.75$

Figure 4. As in Fig. 1 but for the "one element partition" case for a 21 elements array with $d/cT_0 = 0.5$, the total length of the array is $10cT_0$ (as in Figs. 1 and 2).

wavelength at the carrier frequency) there are no GLs within the observation domain. Note that the ERP in Fig. 5(b), for the QM case, is angularly smooth without notable "side-lobes" since only the CBFs corresponding to dominant radiation in the broadside direction ($u \sim 0$) are strongly excited while all other CBFs (further away from the broadside direction) are weakly excited and additionally they have weak magnitude with wide angular spreading (see in Fig. 4(b)). Note though that the "shoulder"-like response on the slops of the ERP in Fig. 5(b) are a trace of the side-lobes of the NB case (compare Fig. 5(a)) that are blurred due to the increased frequency bandwidth of the excitation (see, also, in [3]). Finally, note that the ERP of the NB excitation in Fig. 5(a) is the same as the array factor in the TH case for an array with 21 elements with an inter-element separation of half wavelength [13].

Both of the cases ($\#_n = 0$ and $\#_n > 1$) are undesired since, from the kinematic point of view, they pose difficulties for ERP synthesis due to directional ambiguity ($\#_n > 1$, giving GLs within the observation domain in Fig. 3) or degenerate CBFs ($\#_n = 0$ and possible element's close proximity effects). Consequently, the case of a CBF having only one "main lobe" within the observation domain, $\#_n = 1$, is the most desirable, since: (i) the corresponding contribution is not degenerate, and therefore, may be effectively exploited; and (ii) no possible directional ambiguity is introduced into the ERP (i.e., no GLs as is obtained in Fig. 5).

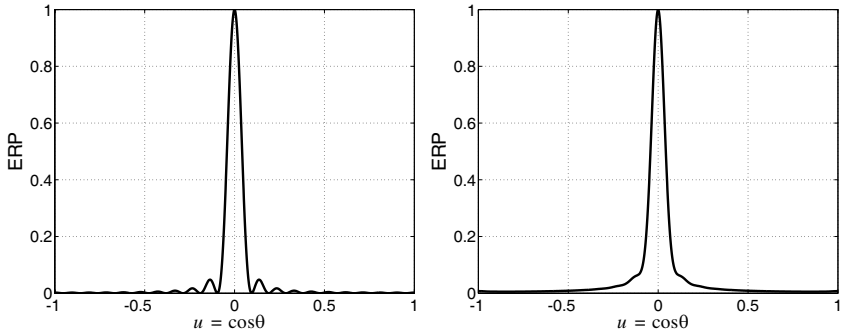

Figure 5. The ERP for a uniformly excited array (equal s_{np}, see in (2), for all elements) with the same physical and waveform parameters that were used for the CBF layout in Fig. 4 for two cases: (a) $T/T_0 \gg 1$, i.e., NB excitation regime; (b) $T/T_0 = 0.75$, i.e., QM excitation regime.

4.1.1. CBF Kinematic-sparsity

Recall that a broadside radiating antenna array is considered as being *sparse* whenever the inter-element spacing $d/cT_0 > 1$ [2, 3]. This condition comes from the fact that for $d/cT_0 > 1$, the peak of the first ERP's grating lobe appears within the observation domain (see, e.g., the examples in Fig. 3). Following the discussion in the last paragraph, various states of sparsity (termed m-sparsity) can be defined so as to generalize the term "array sparsity/sparse array", where sparsity is defined with respect to a measure of the inter element spacing[‖]. To this end, we define an *m-sparse* condition when $d/cT_0 \in (D_m^h, D_{m-1}^h)$, for $0 < m \leq N-1$, and 0-sparse condition for $d/cT_0 \in (D_0^h, \infty)$. This definition indicates that for an m-sparse array, all CBFs with index $m' \geq m$ have $\#_{m'} > 1$, i.e., have more than one dominant beam within the observation domain. In contrast, all CBFs with $m' < m$ have $\#_{m'} = 1$. This case is demonstrated in Figs. 6–7 which depict the CBF layout and corresponding ERP, respectively, for a 13 elements array of size $D = 10cT_0$ as in the previous examples but with $d/cT_0 = 0.83\dot{3}$ and a modulated Lorenzian pulsed waveform that is radiated by each of the elements. The CBF layouts in Fig. 6 demonstrates that for CBFs with index grater than 3 and lower than 22 there is more than one dominant beam within the observation domain whereas all other CBFs have a single dominant beam within the observation domain. This case is therefore identified as "4-sparsity" array. The corresponding ERPs are depicted in Fig. 7. It may clearly observed by comparing Fig. 7 with Fig. 5 ("one element partition" case) that having some CBFs with more than one dominant beam within the observation domain results in somewhat higher side-lobes away from the main beam (see, e.g., Fig. 6(a)). Furthermore, for $|u| \sim 1$ the first GL starts its rise into the observation domain that will become more pronounced for larger inter-element distances (lower *m-sparsity* index) and eventually for $d/cT_0 > 1$ the first GL will fully appear (compare Fig. 3). Note that the emergence of the first GL within the observation domain corresponds to "0-sparse" conditions (see in Figs. 2–3).

To conclude, this discussion on sparsity provides a detailed demonstration of the formation of ERP artifacts that are associated with sparse array realizations (GLs and to lesser extent some side-lobes away from the main beam). This discussion is general in the sense that it is uniformly applicable to QM and NB regimes as well as the TH case where such classical antenna array concepts are well understood [13]. Note that the case of UWB excitation was treated in an alternative

[‖] The issue of sparse realization and array sparsity in transient arrays was discussed in [2, 3, 14].

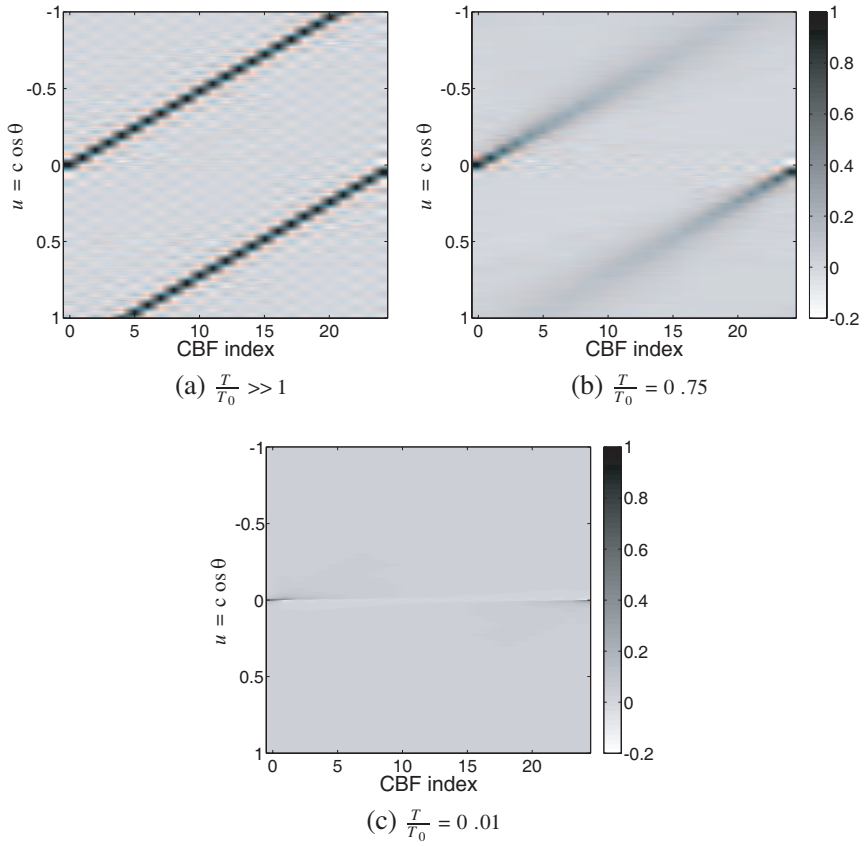

Figure 6. The CBF layout as in Fig. 1 but for the "m-sparsity' case for a 13 elements array with $d/cT_0 = 0.83\dot{3}$ (the total length of the array is $10cT_0$ (as in Figs. 1 and 2)) and for the three excitation regimes: (a) NB (or TH): $T/T_0 \gg 1$; (b) QM: $T/T_0 = 0.75$; and (c) UWB/SP: $T/T_0 = 0.01$.

manner in [3].

Finally and for comparison, Figs. 6(c) and 7(c), respectively, depict the CBF layout and the corresponding ERP for the UWB/SP type of excitation with $T/T_0 = 0.01$ and for the same array parameters as in Figs. 6(a) and 7(a). The CBFs were calculated using the exact expression (Eq. (11)). It can be noted that since, in the UWB/SP regime, the dominant effect is of the narrow short-pulsed envelope (and not of the carrier), the CBFs are decaying fast as a both $|u|$ and the CBF index grows, see in Fig. 6(c). Therefore the ERP is

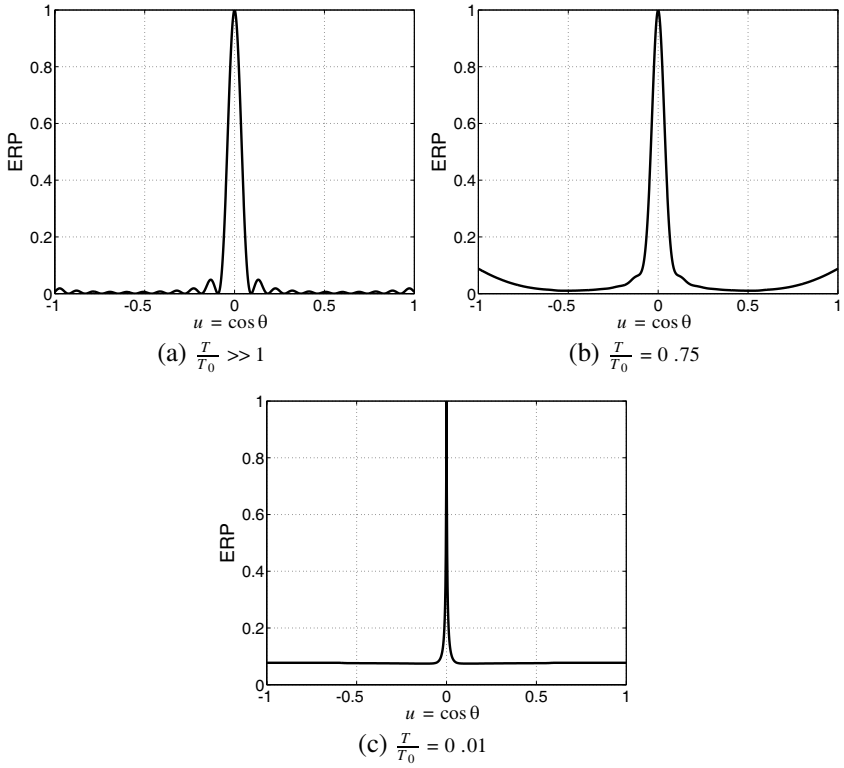

Figure 7. The ERP of a uniformly excited array (equal s_{np}, see in (2), for all elements) with the same physical and waveform parameters used in Fig. 6 for the three excitation regimes: (a) NB (or TH): $T/T_0 \gg 1$; (b) QM: $T/T_0 = 0.75$; and (c) UWB/SP: $T/T_0 = 0.01$.

practically composed by a limited number of CBF contributions that radiates effectively in the broadside direction of which $\lambda_0(u)$ has the most dominant effect. Consequently the ERP for $T/T_0 \ll 1$ (i.e., UWB/SP regime) resembles $\lambda_0(u)$, as can be noted in Fig. 7(c). Note that in this excitation regime, different sparsity considerations should be applied that are based on the pulsed duration T, see the detailed discussion in [3] (and in [14]).

4.2. Waveform-dynamic

Each contributing component in the summation in Eq. (13a) is given by a product of two terms (waveforms) that exhibit dissimilar dominance

behaviors in a different frequency regime. The first term is the pulsed bell-shaped slowly-varying autocorrelation $\mathcal{R}_{r_0}$, which depends on T, while the second term, a much more rapidly-varying carrier, depends on T_0. Hence, the CBFs' behavior in the different bandwidth regimes is governed by an interplay between these terms (controlled by the T/T_0 ratio) as discussed next.

While in the extreme NB regime ($T/T_0 \gg 1$ or in the TH regime), the CBFs of Eq. (13a) can be well approximated by

$$\lambda_n(u) \sim \frac{\mathcal{R}_{r_0}(0)}{\sqrt{2N-1}} \frac{\sin\left((2N-1)\left[\frac{d}{cT_0}u + \frac{n}{2N-1}\right]\pi\right)}{\sin\left(\left[\frac{d}{cT_0}u + \frac{n}{2N-1}\right]\pi\right)}, \tag{18}$$

which can be recognized as a type of Dirichlet interpolation function set (these CBFs are depicted in Figs. 1(a), 2(a), 4(a), and 6(a)). For the NB and QM regimes, the summation in Eq. (18) is difficult to analyze. Applying the Euler-Maclaurin sum formula [15], provides a convenient integral expression of the CBFs for further use to yield

$$\lambda_n(u) = \frac{1}{\sqrt{2N-1}} \int_{1-N}^{N-1} dy\, \mathcal{R}_{r_0}(\mu y) e^{i\xi_n y} + \mathrm{Rem}(u) \tag{19a}$$

$$\begin{aligned}\mathrm{Rem}(u) = \frac{1}{\sqrt{2N-1}} \Bigg\{ & \mathcal{R}_{r_0}\big((N-1)\mu\big)\cos\big((N-1)\xi_n\big) \\ & + 2\int_0^{N-1} dy\, \vartheta(y) \frac{\partial}{\partial y}\big[\mathcal{R}_{r_0}(\mu y)\cos(\xi_n y)\big]\Bigg\},\end{aligned} \tag{19b}$$

where $\vartheta(y) = y - [y] - \frac{1}{2}$ is the sawtooth function, with $[y]$ as the greatest integer smaller than y and $|\vartheta(y)| < \frac{1}{2}$.

The magnitude of the CBFs at the nodes of the CBF-lattice $\{u_{n,l}\}$ is given by

$$\lambda_n(u_{n,l}) = \frac{1}{\sqrt{2N-1}} \sum_{k=1-N}^{N-1} \mathcal{R}_{r_0}(kdc^{-1}u_{n,l}). \tag{20}$$

It can easily be verified that due to the generally decaying bell-shaped envelope of $\mathcal{R}_{r_0}(\tau)$, the ordered sequence of peak values of the CBFs decay as $|u_{n,l} - u_{0,0}|$ grows (with $u_{0,0}$ as the peak of the first CBF, λ_0). To explore this behavior and its dependence on the frequency bandwidth (T/T_0) let us assume, for the sake of simplicity, that $r_0(t) \sim e^{-t^2/2T^2}$ is a Gaussian pulsed envelope giving, $R_{r_0}(\tau) \sim e^{-\tau^2/4T^2}$ (but

other pulsed waveforms can be chosen). Inserting $R_{r_0}(\tau)$ into Eq. (20) and using the Euler-Maclaurin sum formula as in Eq. (19), the relative peak contribution of the CBFs (normalized CBFs) is given by

$$\begin{aligned} \bar{\lambda}_n(u_{n,\ell}) = \frac{\lambda_n(u_{n,\ell})}{\lambda_0(u_{0,0})} &\approx \frac{\sqrt{\pi}}{2}\frac{\mathrm{erf}\,(\Theta)}{\Theta}, \\ \Theta &= \frac{1}{2}\left(\frac{T_0}{T}\right)\left(\ell - \frac{n}{2N-1}\right) \end{aligned} \tag{21}$$

where erf is the error function [16] and $\lambda_0(u_{0,0}) = \frac{2(N-1)}{\sqrt{2N-1}}\sqrt{\pi T} + \mathrm{Rem}(u_{0,0})$, with $|\mathrm{Rem}(u_{n,\ell})| \leq \frac{\sqrt{\pi T}}{\sqrt{2N-1}}$. It should be noted that the function $\mathrm{erf}\,(\Theta)/\Theta$ is a monotonic decreasing function as $|\Theta|$ increases with $\lim_{\Theta\to 0} \mathrm{erf}\,(\Theta)/\Theta = 2/\sqrt{\pi}$ and an asymptotic linear decay, $\lim_{\Theta\to\infty} \mathrm{erf}\,(\Theta)/\Theta = 0$. For the extreme NB case ($T/T_0 \gg 1$), it can be seen that $\bar{\lambda}_n(u_{n,\ell}) = 1$ for all $n \in \mathcal{N}$ and $\ell \in \mathbb{Z}$, i.e., all CBFs have the same relative peak magnitude, which is also evident from their expression in Eq. (18). On the other hand, for pulse excitation within the lower NB and QM regimes, $T/T_0 \lesssim \mathcal{O}(1)$ where $\Theta > 0$, it follows that for a given n and ℓ, $\bar{\lambda}_n(u_{n,\ell})$ is a decreasing function with decreasing T/T_0 (an increase in the excitation bandwidth). Furthermore, for a given n and T/T_0, $\bar{\lambda}_n(u_{n,\ell})$ decreases as $|\ell|$ increases [see, e.g., Eq. (21)]. For the array's ERP, this last observation suggests that if, in addition, the array's physical parameters are, also, set such that $\#_{n_m} > 1$ (n_m-sparse array) and in particular, for the case of 0-sparsity where there are some GLs within the observation domain, the peak magnitude of these GLs decay away from the main radiation beam ¶. In the UWB case where $T/T_0 \to 0$, (limiting case of the above discussion), only the zeroth CBF ($n = 0$) contributes dominantly while $\bar{\lambda}_n(u_{n,\ell})$ is negligibly small for all (n, ℓ) pairs that are different from $(0, 0)$. Different choices of pulsed waveforms (other than Gaussian) give similar results as can be noted via the CBF layouts in Figs. 1, 2, 4, and 6 for the Lorenzian pulse. The difference between different pulsed waveforms is in the decay rate of the CBFs peaks (the erf term in Eq. (21) is replaced by an alternative term).

4.2.1. CBF Partitioning and Sparsity

The discussion on kinematics in Section 4.1 was based on the the array's layout and carrier frequency without applying any waveform

¶ Recall that this decay of the GLs, also discussed in [2, 3], from an alternative point of view.

considerations. The addition of the waveform-dynamic implies that the CBF partitioning and sparsity can be modified in view of the associated waveform effects. To that end, note that the peak magnitude of the CBFs, $\lambda_n(u_{n,l})$, decays as the indexes $(n, |\ell|)$ grow (see, e.g., Figs. 1(b), 2(b), 4(b), and 6(b)) and introduce a threshold parameter $\varepsilon \leq 1$. Next, any normalized with respect to $\lambda_0(0)$ CBF contribution which is $\leq \varepsilon$ can be considered as having a negligible effect on the ERP. By accounting for only non-negligible contributions, the partition of the CBF-lattice (Section 4.1) and the sparsity categorization can be redefined with respect to ε to yield the (n_m, ε)-*sparsity* in a similar manner to that discussed in Section 4.1.1. To demonstrate this term refer to Section 4.1 where it was shown that the CBF layout in Fig. 4(b) belongs to a "one element partition". Setting a high enough ε, the contribution of CBFs with index around 20 can be neglected, hence setting the array realization to that of an "empty partition" *with respect to* ε for some CBFs. Similarly, consider a realization that based on purely kinematic arguments is found as having "more than one element partition" and consequently being sparse. Thresholding the CBFs may reset them to constitute different partition and hence change the array's sparsity condition.

Note that: (i) This discussion is applicable for UWB/SP and QM excitations whereas NB excitation is insensitive to waveform considerations; (ii) The analysis can be applied for the $P \neq 0$ case where various states of sparsity with respect to the excitation parameters are expected to generalize the discussion in [3]; and (iii) (n_m, ε)-sparsity can be applied upon comparing several array realizations or on assessing the robustness of the array's performance to noise and uncertainty in the parameters.

4.3. Numerical Efficient ERP Evaluation

The CBF decomposition discussed above can be used for applications in analysis, synthesis and optimization. One such application is the efficient, repetitive, evaluation of the ERP or, similarly, the simultaneous calculation of the ERP for many array excitation sequences. To this end, let us assume that the array layout and type of excitation pulse is given and the ERP is needed for different sets of excitation weights [different $\{s_{np}\}$ sets, where here we consider the $p = 0$ case]. In that case, the set of CBFs can be calculate in advance by Eq. (13) for a given set of N_θ dirctions and stored in a matrix $\mathcal{T}$ whose size in $N_\theta \times (2N-1)$ for which it's (i,j)th element, $i = 1, \ldots, N_\theta$ and $j = 1, \ldots, 2N-1$, is $\mathcal{T}_{i,j} = \lambda_j(\cos\theta_i)$. The matrix $\mathcal{T}$ represents the layout of the CBFs as depicted in Figs. 1, 2, 4, and 6 for $N_\theta = 1001$. Next, following Eq. (12), the ERP is obtained by multiplying $\mathcal{T}$ with a

matrix $\mathcal{S}_g$ whose size is $(2N-1)\times N_s$ where N_s is the number of array realizations and each of its columns is the vector containing the square of the absolute magnitude of the DFT coefficients of a zero padded sequence of N array weights (of one of the possible N_s realizations). Note, that $\mathcal{T}$ is the transformation (mapping) matrix between the sets of discrete array weights to the discrete sets of ERP values: $\mathcal{E}_a = \mathcal{T}\times\mathcal{S}_g$ (of size $N_\theta \times N_s$). It should also be noted that once $\mathcal{T}$ was calculated by a fast Fourier transform (FFT, see in Eq. (13) or Eq. (11) and the discussion in Section 3.2.1), with a computational complexity of $\sim \mathcal{O}(N_\theta N \log N)$ operations, the ERP evaluation at N_θ directions costs the evaluation of $\mathcal{S}_g$ (costs approximately $N_s N \log N$ operations for large N) and the matrix vector product that costs approximately $\mathcal{O}(N_s N_\theta N)$ operations. For comparison, the direct computation via Eq. (6) costs $\mathcal{O}(N_s N_\theta N^2)$, which is more numerically expensive than the CBF based calculation (via Eq. (12)) for large number of array elements and array realizations.

5. SUMMARY AND CONCLUSIONS

A set of CBFs for the mathematical formulation of the ERP of a short-pulsed transient linear array was derived. Upon defining sets of (*i*) layout parameters (geometry, type of radiating elements) and (*ii*) pulsed excitation waveforms that can be radiated by the array, the set of CBF elements form a mapping between the "energy" of the DFT coefficients of the excitation sequence and the far-field ERP. Though the CBFs are the basic building blocks of the ERP, by themselves they do not represent a valid realizable energy radiation pattern. Considering the CBF set directional (spectral, u-dependent) characteristics, gives rise to a reformulation of the general term of TH *array sparsity* to incorporate for various states of sparsity. Moreover, it provides a complementary point of view (waveform or CBF motivated) of sparsity for TTD arrays. Theses concepts were, also, demonstrated for several array realizations.

As a concluding remark, the representation of the radiation pattern by the CBFs as in Eq. (12) can be applied for an array analysis or as an efficient mechanism for array synthesis. In analysis the CBF formulation can be employed for an efficient ERP calculation with *numerically low complexity* (Section 4.3) or as a tool for establishing bounds on array performance vis-à-vis the relationship between the CBF elements. In an ERP synthesis problem for achieving prescribed characteristics or in an inverse source problem, the CBF formulation provides simple means for controlling the ERP. These issues will be explored in a different communication.

ACKNOWLEDGMENT

This research was supported by The Israel Science Foundation (Grant No. 745/07).

REFERENCES

1. Harmuth, H. F. (ed.), *Antennas and Waveguides for Nonsinusoidal Waves*, Advances in Electronics & Electron Physics Supplement, Academic Press, 1984.
2. Shlivinski, A. and E. Heyman, "A unified kinematic theory of transient arrays," *Ultra-Wideband, Short-pulse Electromagnetics*, P. Smith and S. R. Cloude (eds.), Vol. 5, 11–20, Plenum Press, NY, 2002.
3. Shlivinski, A., "Kinematic properties of short-pulsed sparse transmitting arrays properties of short-pulsed sparse transmitting arrays," *Progress In Electromagnetics Research*, Vol. 115, 11–33, 2011.
4. Davis, P. J., *Circulant Matrices*, Pure & Applied Mathematics, Wiley-Interscience, 1979.
5. Ferreira, P. J. S. G., P. Jorge, and S. G. Ferreira, "Localization of the eigenvalues of toeplitz matrices using additive decomposition, embedding in circulants, and the fourier transform," *Proc. 10th IFAC Symposium on System Identification SYSID'94*, 271–276, 1994.
6. Tee, G. J., "Eigenvectors of block circulant and alternating circulant matrices," *Res. Lett. Inf. Math. Sci.*, Vol. 8, No. 6, 123–142, 2005.
7. Ziolkowski, R. W., "Properties of electromagnetic beams generated by ultra-widebandwidth pulse-driven arrays," *IEEE Transactions on Antennas and Propagation*, Vol. 40, No. 8, 888–905, 1992.
8. Shlivinski, A. and E. Heyman, "Time-domain near-field analysis of short-pulse antennas — Part I: Spherical wave (multipole) expansion," *IEEE Transactions on Antennas and Propagation*, Vol. 47, No. 2, 271–279, 1999.
9. Ciattaglia, M. and G. Marrocco, "Investigation on antenna coupling in pulsed arrays," *IEEE Transactions on Antennas and Propagation*, Vol. 54, 835–843, Mar. 2006.
10. Marrocco, G. and G. Galletta, "Hermite-Rodriguez UWB circular arrays," *IEEE Transactions on Antennas and Propagation*, Vol. 58, 381–390, Feb. 2010.

11. Horn, R. and C. Johnson, *Topics in Matrix Analysis*, Cambridge University Press, 1986.
12. Oppenheim, A. V., R. W. Schafer, and J. R. Buck, *Discrete-Time Signal Processing*, 2nd edition, Prentice-Hall Signal Processing Series, 1999.
13. Balanis, C., *Antenna Theory, Analysis and Design*, 3rd edition, John Wiley & Sons, Inc., Wiley Intersience, Hoboken, New Jersey, 2005.
14. Schwartz, J. L. and B. D. Steinberg, "Ultrasparse, ultrawideband arrays," *IEEE Transactions on UFFC*, Vol. 45, 376–393, Mar. 1998.
15. Apostol, T. M., *Calculus*, Vol. 2, Blaisdell, New York, 1969.
16. Gradshteyn, I. S. and I. M. Ryzhik, *Table of Integral, Series, and Products*, 5th edition, Academic Press, 1994.